PAPER

Check for updates

Fluorinated dibenzo[a,c]-phenazine-based green to red thermally activated delayed fluorescent OLED emitters†

Gloria Hong, [iD] ‡[a] Changfeng Si, [iD] ‡[b] Abhishek Kumar Gupta, [iD] ‡[bc]
Claudia Bizzarri, [iD] [a] Martin Nieger, [iD] [d] Ifor D. W. Samuel, [iD] *[c]
Eli Zysman-Colman [iD] *[b] and Stefan Bräse [iD] *[ae]

Purely organic thermally activated delayed fluorescence (TADF) emitting materials for organic light-emitting diodes (OLEDs) enable a facile method to modulate the emission color through judicious choice of donor and acceptor units. Amongst purely organic TADF emitters, the development of TADF molecules that emit at longer wavelengths and produce high-efficiency devices that show low efficiency roll-off remains a challenge. We report a modular synthesis route that delivers three structurally related fluorinated dibenzo[a,c]-phenazine-based TADF molecules, each bearing two donor moieties with different electron-donating strengths, namely 3,6-bis(3,6-di-*tert*-butyl-9H-carbazol-9-yl)-10-fluorodibenzo[a,c]phenazine (**2DTCz-BP-F**), 3,6-bis(9,9-dimethylacridin-10(9H)-yl)-10-fluorodibenzo[a,c]-phenazine (**2DMAC-BP-F**) and 10,10′-(10-fluorodibenzo[a,c]phenazine-3,6-diyl)bis(10H-phenoxazine) (**2PXZ-BP-F**). They exhibit donor strength-controlled color-tuning over a wide color range from green to deep-red with photoluminescence maxima, λ_{PL}, of 505 nm, 589 nm, and 674 nm in toluene solution. OLED devices using these TADF materials showed excellent to moderate performance with an EQE$_{max}$ of 21.8% in the case of **2DMAC-BP-F**, 12.4% for **2PXZ-BP-F** and 2.1% with **2DTCZ-BP-F**, and associated electroluminescence (EL) emission maxima, λ_{EL}, of 585 nm, 605 nm and 518 nm in an mCBP host, respectively.

Introduction

Among the emitting materials for use in organic light-emitting diodes (OLEDs), purely organic thermally activated delayed fluorescence (TADF) emitters have drawn intense interest in

[a] *Institute of Organic Chemistry, Karlsruhe Institute of Technology (KIT), Fritz-Haber-Weg 6, 76131 Karlsruhe, Germany. E-mail: stefan.braese@kit.edu*

[b] *Organic Semiconductor Centre, EaStCHEM School of Chemistry, University of St Andrews, St Andrews, Fife, KY16 9ST, UK. E-mail: eli.zysman-colman@st-andrews.ac.uk; Fax: +44 (0)1334 463808; Tel: +44 (0)1334 463826*

[c] *Organic Semiconductor Centre, SUPA School of Physics and Astronomy, University of St Andrews, St Andrews, Fife, KY16 9SS, UK. E-mail: idws@st-andrews.ac.uk; Fax: +44 (0)1334 463104; Tel: +44 (0)1334 463826*

[d] *Department of Chemistry, University of Helsinki, P. O. Box 55, 00014 Finland*

[e] *Institute of Biological and Chemical Systems (IBCS-FMS), Karlsruhe Institute of Technology (KIT), Hermann-von-Helmholtz-Platz 1, 76344 Eggenstein-Leopoldshafen, Germany*

† Electronic supplementary information (ESI) available: General information, experimental procedures, compound characterization. CCDC 2086119 (**2DMAC-BP-F**). For ESI and crystallographic data in CIF or other electronic format see DOI: 10.1039/d1tc04918f

‡ Authors contributed equally to this work.

recent years as they enable devices to reach a theoretical internal quantum efficiency (IQE) of 100%. This is possible through efficient harvesting of both singlet and triplet excitons to produce light, the latter of which are converted to the former *via* reverse intersystem crossing (RISC). Organic TADF emitters do not contain scarce, noble metals that are extracted through environmentally damaging mining operations. Swift progress has been reported in the development of purely organic TADF emitters and now there are numerous examples of TADF OLEDs showing comparable efficiencies to phosphorescent devices.[1,2]

RISC at ambient temperatures occurs in organic compounds that possess a small energy gap, ΔE_{ST}, between the lowest-lying singlet state S$_1$ and triplet state T$_1$, and show non-zero spin–orbit coupling (SOC).[3] For this scenario to occur, there must be a spatial separation of the electron-donating unit accommodating the highest-occupied molecular orbital (HOMO) and the electron-accepting unit hosting the lowest-unoccupied molecular orbital (LUMO).[4] The implementation of this donor–acceptor molecular design produces a strong charge-transfer (CT) character of the S$_1$ state.[3]

The design of TADF materials that emit at longer wavelengths poses some unique challenges for maintaining a high

This journal is © The Royal Society of Chemistry 2022

J. Mater. Chem. C, 2022, **10**, 4757–4766 | **4757**

photoluminescence quantum yield (Φ_{PL}). The Φ_{PL} is dependent on the rate constant of radiative decay processes such as fluorescence, but also nonradiative decay processes such as internal conversion (IC) and intersystem crossing (ISC).[5] In large, aromatic molecules, where the electronic relaxation lies within the rule of a weak coupling limit as reported by Englman and Jortner,[6] the rate constant of the nonradiative decay, k_{nr}, is inversely proportional to the exponential of the optical energy gap ΔE_{opt}. In contrast, the rate constant of the radiative decay, k_r, is proportional to the cube of ΔE_{opt}.[5,7,8] As the energy of the emissive excited state decreases, the influence of nonradiative decay increases exponentially because the vibronic coupling between the excited state and ground state is facilitated. The challenge of reducing losses due to vibrational quenching and other nonradiative decay pathways in TADF molecules emitting at longer wavelengths can be partially addressed by introducing rigidity into the molecular structure of the donor and acceptor units. Common acceptors for purely organic TADF emitters are aromatic ketones such as anthraquinones, naphthalimides, or

heteroaromatic systems like quinoxaline and dibenzo[a,c]phenazine (BP).[9] These acceptors show deep LUMO levels of -3.4 eV,[10] -2.99 eV,[11] -2.81 eV,[12] and -2.90 eV,[13] respectively, that contribute to stabilizing the S_1 state and are therefore beneficial for use in the design of TADF emitters targeting longer wavelength regions.

Zhao and co-workers first reported TADF compounds bearing the BP acceptor, which exhibits a rigid, large π-conjugated system.[14] These compounds contain one to three donor moieties in the donor–acceptor or poly(donor)–acceptor strategy, which are commonly applied for TADF molecule design. The greater number of 9,9-dimethyl-9,10-dihydroacridine (DMAC) donors was expected to strengthen the intramolecular charge transfer (ICT) and lead to color-tuning from green to orange-red emission with electroluminescence maxima, λ_{EL}, of 560 nm, 576 nm, and 606 nm for devices featuring **1DMAC-BP**, **2DMAC-BP**, and **3DMAC-BP**, respectively (Fig. 1). A maximum external quantum efficiency (EQE_{max}) of 22.0% was observed for the OLED device with **3DMAC-BP** doped in mCBP (18 wt%) at 606 nm.
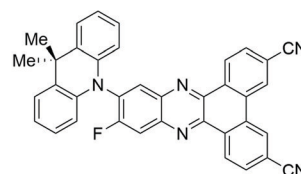

1DMAC-BP: R = R' = H
2DMAC-BP: R = DMAC, R' = H
3DMAC-BP: R = R' = DMAC

λ_{EL} = 560 nm, 576 nm, 606 nm
λ_{PL} = 549 nm, 565 nm, 590 nm
Φ_{PL} = 42%, 84%, 89%
ΔE_{ST} = 0.22 eV, 0.21 eV, 0.05 eV
τ_d = 12.6 μs, 7.5 μs, 2.9 μs
EQE_{max} = 10.1%, 11.8%, 22.0%
ACS Appl. Mater. Interfaces **2019**, *11*, 26144–26151.

1PXZ-BP: R = R' = H
2PXZ-BP: R = PXZ, R' = H
3PXZ-BP: R = R' = PXZ

λ_{EL} = 590 nm, 606 nm, 634 nm
λ_{PL} = 578 nm, 596 nm, 630 nm
Φ_{PL} = 73%, 63%, 22%
ΔE_{ST} = 0.25 eV, 0.10 eV, 0.03 eV
τ_d = 4.8 μs, 4.3 μs, 2.0 μs
EQE_{max} = 26.3%, 19.2%, 7.1%
Adv. Electron. Mater. **2020**, *6*, 1900843.

FBPCNAc

λ_{EL} = 597 nm
λ_{PL} = 607 nm
Φ_{PL} = 79%
ΔE_{ST} = 0.047 eV
τ_d = 11.1 μs
EQE_{max} = 23.8%
ACS Appl. Mater. Interfaces **2020**, *12*, 16, 18730–18738.

TAT-FDBPZ

λ_{EL} = 611 nm
λ_{PL} = 593 nm
Φ_{PL} = 62%
ΔE_{ST} = 0.10 eV
τ_d = 1.51 μs
EQE_{max} = 9.2%
ACS Appl. Mater. Interfaces **2020**, *12*, 30652–30658.

This work:

2PXZ-BP-F: R = PXZ
2DMAC-BP-F: R = DMAC
2DTCz-BP-F: R = DTCz

λ_{EL} = 605 nm, 585 nm, 518 nm
λ_{PL} = 611 nm, 584 nm, 522 nm
Φ_{PL} = 58%, 78%, 60%
ΔE_{ST} = 0.02 eV, 0.11 eV, 0.30 eV
τ_d = 1.83 μs, 90.6 μs, 10.1 ms
EQE_{max} = 12.4%, 21.8%, 2.1%

PXZ

DMAC

DTCz

Fig. 1 BP-based TADF emitters; DMAC: 9,9-dimethyl-9,10-dihydroacridine, PXZ: 10H-phenoxazine, DTCz: 3,6-di-*tert*-butylcarbazole.

4758 | *J. Mater. Chem. C*, 2022, **10**, 4757–4766

This journal is © The Royal Society of Chemistry 2022

By employing the stronger donor 10H-phenoxazine (PXZ), the λ_{EL} for the devices with **1PXZ-BP**, **2PXZ-BP**, and **3PXZ-BP** were red-shifted to 590 nm, 606 nm, and 634 nm, respectively. The most efficient device with **1PXZ-BP** as the emitter showed an EQE_{max} of 26.3% (7 wt% doped in CBP).[13] Both Lee and coworkers as well as Wang and coworkers, have reported fluoro-substituted BP acceptors intending to strengthen the acceptor with the presence of the strongly inductively electron-with-drawing fluorine substituent.[15,16] Lee and coworkers reported the use of a fluorine substituent at the acceptor moiety in the ortho-position (**FBPCNAc**, Fig. 1) to the donor moiety. **FBPCNAc** is brightly luminescent in 1 wt% doped polystyrene film with λ_{PL} = 607 nm, a Φ_{PL} of 79% and a delayed lifetime of τ_d = 11.1 μs. In the electroluminescent (EL) device, it showed an emission maximum of λ_{EL} = 597 nm, an EQE_{max} of 23.8% and low efficiency roll-off. Wang and coworkers on the other hand, attached two fluorine substituents in 11- and 12-position to the BP acceptor on the opposite side of the donor moieties in 3- and 6-position (**TAT-FDBPZ**, Fig. 1) and observed that the introduc-tion of the fluorine substituents led to a stronger ICT state and a red-shifted emission. The emission of the 20 wt% doped CBP films of the fluorinated **TAT-FDBPZ** is bathochromically shifted from λ_{PL} = 593 nm by 17 nm in comparison to its non-fluorinated analogue (λ_{PL} = 576 nm). However, this came at the cost of a slightly decreased Φ_{PL} from 76% to 62%. The τ_d of **TAT-FDBPZ** is 1.51 μs, which is shorter than for the non-fluorinated analog where τ_d = 2.30 μs. The device based on **TAT-FDBPZ** showed λ_{EL} of 611 nm and an EQE_{max} of 9.2%.

Building on these findings, we aimed to reduce the mole-cular weight of the emitter in the context of vacuum-deposited device fabrication. We investigated a compromise of the poly(donor)–acceptor strategy by installing two donor units and an electron-withdrawing fluorine substituent to strengthen the dibenzo[a,c]phenazine acceptor. We designed three new TADF emitters, shown in Fig. 1, based on 10-fluorodibenzo-[a,c]phenazine (**BP-F**), each incorporating two donor moieties, namely 3,6-bis(3,6-di-tert-butyl-9H-carbazol-9-yl)-10-fluorodibenzo-[a,c]phenazine (**2DTCz-BP-F**), 3,6-bis(9,9-dimethylacridin-10(9H)-yl)-10-fluorodibenzo[a,c]phenazine (**2DMAC-BP-F**) and 10,10′-(10-fluorodibenzo[a,c]phenazine-3,6-diyl)bis(10H-phenoxazine) (**2PXZ-BP-F**). We successfully applied a modular synthesis strategy that allowed for the facile synthesis of these TADF molecules. The compounds show color tuning based on the choice of donor, emitting from green to deep-red for **2DTCz-BP-F**, **2DMAC-BP-F**, and **2PXZ-BP-F** at peak wavelengths, λ_{PL}, of 505 nm, 589 nm, and 674 nm in toluene solution, respectively. **2DMAC-BP-F** and **2PXZ-BP-F** show small ΔE_{ST} of 0.11 eV and 0.02 eV while using the weakest **DTCz** donor resulted in a compound **2DTCz-BP-F** showing the largest ΔE_{ST} of 0.30 eV in doped mCBP film (5 wt% **2DTCz-BP-F**, 10 wt% **2DMAC-BP-F**, and 1.5 wt% **2PXZ-BP-F**). The corresponding delayed lifetimes follow the trend in ΔE_{ST} at 90.6 μs, 1.83 μs and 10.152 ms, respectively, for **2DMAC-BP-F**, **2PXZ-BP-F** and **2DTCz-BP-F**. The OLEDs fabricated with **2DMAC-BP-F**, **2PXZ-BP-F** and **2DTCz-BP-F** exhibited EQE_{max} of 21.8%, 12.4% and 2.1% at λ_{EL} of 585 nm, 605 nm and 518 nm, respectively.

Results and discussion

Molecular design and synthesis

The synthesis of the **2D-BP-F** (D = PXZ, DMAC, DTCz) family of emitters is outlined in Scheme 1. Firstly, 3,6-dibromo-10-fluorodibenzo[a,c]phenazine **3** was synthesized through a con-densation reaction of 3-fluorobenzene-1,2-diamine **1** and 3,6-dibromophenantrene-9,10-dione **2** in acetic acid and ethanol at elevated temperatures. Proceeding from intermediate **3**, the target compounds **2DTCz-BP-F**, **2DMAC-BP-F** and **2PXZ-BP-F** were obtained through Pd-catalyzed Buchwald–Hartwig cross-coupling reactions in excellent yields. While the catalyst system $Pd(OAc)_2/P(tBu)_3$ gave excellent yields for the synthesis of **2DTCz-BP-F** and **2DMAC-BP-F**, the catalyst system $Pd(dba)_2/(tBu)_3PHBF_4$ gave higher yields for the synthesis of **2PXZ-BP-F**.

The three emitters were purified further by gradient-temperature sublimation. The chemical structure and purity of the three compounds were confirmed using ^{1}H, ^{13}C, and ^{19}F nuclear magnetic resonance (NMR) spectroscopy, high-resolution mass spectrometry (HRMS), infrared spectroscopy, melting point analysis, and elemental analysis (EA). A single crystal suitable for X-ray diffraction analysis was obtained for **2DMAC-BP-F** by evaporating a solution in deuterated benzene in an NMR tube at room temperature (Fig. 2a). Analysis of the crystal structure of **2DMAC-BP-F** showed that the fluorine atom is disordered about a mirror plane. The DMAC donor units are strongly twisted with a dihedral angle of 65° to the BP acceptor. The DMAC donors display an almost planar conformation with the quaternary carbon being pushed out of the plane by 0.11 Å while the two benzene rings of the DMAC are tilted towards each other by 4°. Crystals of **2DTCz-BP-F** were obtained by evaporation of a solution in deuterated chloroform in an NMR tube at room temperature (Fig. 2b). Four crystallographi-cally independent molecules were found with the fluorine atoms disordered about a mirror plane and the donor units strongly twisted with an average dihedral angle of 46.6°. Crystallographic data of both molecules are quoted in the ESI† (Table S1).

Theoretical calculations

The ground-state geometries of **2DTCz-BP-F**, **2DMAC-BP-F**, and **2PXZ-BP-F** were optimized using density functional theory (DFT) at the PBE0/6-31G(d,p) level of theory in the gas phase.[17,18] The excited state properties were calculated by time-dependent density functional theory (TD-DFT) within the Tamm–Dancoff approximation (TDA-DFT) based on the opti-mized ground-state geometries.[19] The calculated energy levels of the highest occupied molecular orbits (HOMOs) and lowest unoccupied molecular orbits (LUMOs) are presented in Fig. 3, and the results are summarized in Table S2 (ESI†). The dihedral angles between the donor and acceptor moieties were found to be around 48.6° and 47.6° for **2DTCz-BP-F**, 87.9°, and 90.1° for **2DMAC-BP-F** and 85.9° and 72.2° for **2PXZ-BP-F**, respectively. In comparison with the value obtained from the crystal structure, the dihedral angle between the DMAC and the BP-F groups in **2DMAC-BP-F** (65°) was found to be smaller than that

Scheme 1 Synthesis of **2DTCz-BP-F**, **2DMAC-BP-F**, and **2PXZ-BP-F**.

Fig. 2 (a) Molecular structure of **2DMAC-BP-F** (solvent and one disordered F-position omitted for clarity, displacement parameters are drawn at 30% probability level); (b) the molecular structure of one of the crystallographically independent molecules of **2DTCz-BP-F** (solvent and minor disordered F-position omitted for clarity, displacement parameters are drawn at 30% probability level).

theoretically calculated, while the average dihedral angle between the DTCz and the BP-F groups in **2DTCz-BP-F** (46.6°) was in good accordance with the calculated value. Due to the almost orthogonal conformations of **2DMAC-BP-F** and **2PXZ-BP-F**,

the HOMO and LUMO distributions are localized on the donor and acceptor moieties, respectively, in both molecules, which results in small ΔE_{ST}. The LUMOs of all three compounds are distributed over the BP-F acceptor core, while the HOMOs are

4760 | *J. Mater. Chem. C*, 2022, **10**, 4757–4766
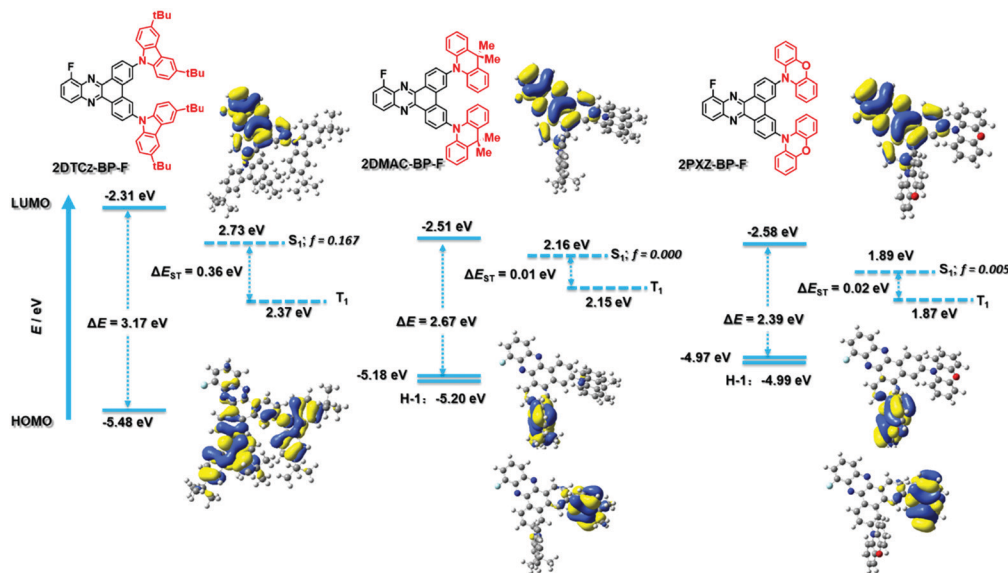
This journal is © The Royal Society of Chemistry 2022

Fig. 3 Theoretical modeling of the energies of the HOMO/LUMO orbitals and the S_1 and T_1 states and oscillator strength of **2DTCz-BP-F**, **2DMAC-BP-F**, and **2PXZ-BP-F** and the electron density distribution (ISO value = 0.02) of the frontier molecular orbitals.

generally located on the donor moieties. In the case of **2DTCz-BP-F**, the HOMO is mainly localized on both of the 3,6-di-*tert*-butyl-9*H*-carbazole (DTCz) units, whereas for **2DMAC-BP-F** or **2PXZ-BP-F**, the HOMO is mainly found on only one of the donor units while HOMO-1 is localized on the other donor as these two orbitals are pseudo degenerate (Fig. 3). The HOMO–LUMO gap, $\Delta E_{\text{HOMO–LUMO}}$, decreases from 3.17 eV for **2DTCz-BP-F** to 2.67 eV for **2DMAC-BP-F** and 2.39 eV for **2PXZ-BP-F**, following a trend of decreasing $\Delta E_{\text{HOMO–LUMO}}$ with increasing donor strength. The oscillator strength, f, for the transition from S_0 to S_1 was found to be 0.167, 0, and 0.005 for **2DTCz-BP-Fz**, **2DMAC-BP-F**, and **2PXZ-BP-F**, respectively, which reflects the significantly greater orbital overlap due to the less twisted conformation and weaker nature of the DTCz donor. The S_1 energies are 2.73 eV for **2DTCz-BP-F**, 2.16 eV for **2DMAC-BP-F**, and 1.89 eV for **2PXZ-BP-F**, while the T_1 energies decrease from 2.37 eV, 2.15 eV, and 1.87 eV, respectively, following a similar trend to that observed for $\Delta E_{\text{HOMO–LUMO}}$. The clear spatial separation of the frontier orbitals in **2DMAC-BP-F** and **2PXZ-BP-F** results in a very small ΔE_{ST} of less than 0.02 eV, while the larger overlap between HOMO and LUMO for **2DTCz-BP-F** leads to a ΔE_{ST} of 0.36 eV.

Electrochemistry

Cyclic voltammetry (CV) was performed to determine the HOMO and LUMO levels of the emitters. The oxidation and reduction potentials of the emitters were evaluated in Ar-saturated dichloromethane (DCM) solution with tetrabutyl-ammonium hexafluorophosphate as the supporting electrolyte. The values are reported *versus* standard calomel electrode (SCE). The results obtained from the CV measurements are summarized in Table 1.

As shown in Fig. 4, all three compounds show reversible oxidation and reduction processes. The main oxidation waves occur at 0.80 V, 1.00 V, and 1.32 V for **2PXZ-BP-F**, **2DMAC-BP-F**,

Table 1 Summary of the results obtained through cyclic voltammetry

Emitter	$E_{\text{ox}}{}^a$ [V *vs.* SCE]	$E_{\text{red}}{}^a$ [V *vs.* SCE]	$E_{\text{HOMO}}{}^b$ [eV]	$E_{\text{LUMO}}{}^b$ [eV]	$\Delta E_{\text{H–L}}{}^c$ [eV]
2PXZ-BP-F	0.80	−1.21	−5.14	−3.13	2.01
2DMAC-BP-F	1.00	−1.19	−5.34	−3.15	2.20
2DTCz-BP-F	1.32	−1.18	−5.66	−3.16	2.50

[a] In Ar-saturated DCM (0.1 M $[n\text{Bu}_4\text{N}]\text{PF}_6$) at a scan rate of 100 mV s^{-1}. $E_{\text{ox/red}}$ [V *vs.* SCE] = $E_{\text{ox/red}}$ [V *vs.* Fc/Fc$^+$] + 0.46.[20] [b] The HOMO and LUMO energies were determined using $E_{\text{HOMO/LUMO}} = -(E_{\text{ox}}/E_{\text{red}} + 4.8)$ eV where E_{ox} and E_{red} are anodic and cathodic peak potentials, respectively, *versus* Fc/Fc$^+$.[21–23] [c] $\Delta E_{\text{H–L}} = |E_{\text{HOMO}} - E_{\text{LUMO}}|$.

and **2DTCz-BP-F**, respectively. These are each assigned to the oxidation of PXZ, DMAC, and DTCz, and reflect the relative strength of the donors. **2DMAC-BP-F** shows an additional minor oxidation wave at 0.77 V, which is characteristic of the redox behavior of DMAC-containing compounds.[24] The respective HOMO levels are −5.14 eV, −5.34 eV, and −5.66 eV for **2PXZ-BP-F**, **2DMAC-BP-F**, and **2DTCz-BP-F**. The reduction waves occur at very similar potentials of −1.21 V, −1.19 V, −1.18 V for **2PXZ-BP-F**, **2DMAC-BP-F**, and **2DTCz-BP-F**, respectively, and indicate that the electronic coupling between the donor and acceptor moiety is small.

The corresponding redox gaps, $\Delta E_{\text{H–L}}$, decrease from 2.50 V to 2.20 V and 2.01 V for **2DTCz-BP-F**, **2DMAC-BP-F**, and **2PXZ-BP-F**, respectively matches the HOMO–LUMO gap trend predicted by DFT calculations.

Photophysical properties

The UV-vis absorption spectra of the three emitters in dilute toluene are shown in Fig. 5a, and the photophysical properties are summarized in Table 2. All three compounds exhibit strong absorption bands at around 310 nm, which can be attributed to locally excited (LE) $\pi-\pi^*$ transitions of the donors and BP-F

This journal is © The Royal Society of Chemistry 2022

J. Mater. Chem. C, 2022, **10**, 4757–4766 | **4761**

Fig. 4 Cyclic voltammograms of **2PXZ-BP-F**, **2DMAC-BP-F**, and **2DTCz-BP-F** in Ar-saturated DCM solution (0.1 M [nBu$_4$N][PF$_6$]) at a scan rate of 100 mV s^{-1}.

moieties, respectively.[24–26] Weaker and broad absorption bands are observed from 410 to 520 nm, which are assigned to ICT transitions from the donor units to the acceptor core.[27] This latter band is more intense for **2DTCz-BP-F** (λ_{abs} = 440 nm, 21 × 10^3 M^{-1} cm^{-1}) compared to those of **2DMAC-BP-F** (λ_{abs} = 415 nm, 3 × 10^3 M^{-1} cm^{-1}) and **2PXZ-BP-F** (λ_{abs} = 476 nm, 3 × 10^3 M^{-1} cm^{-1}) as the DTCz groups adopt a less twisted conformation, leading to greater conjugation and greater oscillator strength for the ICT transitions in **2DTCz-BP-F**, values that are corroborated by the DFT calculations (Fig. S12–S17, ESI†). There is the expected shift to lower energies of the ICT band across the family of compounds that is aligned with increasing donor strength. All compounds exhibit unstructured and broad PL spectra in toluene (Fig. 5a), indicative of an excited state with strong ICT character, with peak maxima, λ_{PL}, at 505 nm, 589 nm, and 674 nm for **2DTCz-BP-F**, **2DMAC-BP-F**, and **2PXZ-BP-F**, respectively. Positive solvatochromism is observed for all compounds (Fig. 5a and Table S3, ESI†), which is

consistent with the CT nature of the emissive excited state. The optical bandgaps, E_g, calculated from the normalized absorption and emission spectra intersection point, are 2.60 eV, 2.32 eV, and 2.13 eV for **2DTCz-BP-F**, **2DMAC-BP-F**, and **2PXZ-BP-F**, respectively. Except for **2DTCz-BP-F** (E_g = 2.60 eV *vs.* $E_{S1\,theory}$ = 2.73 eV), experimental E_g for **2DMAC-BP-F** (E_g = 2.32 eV *vs.* $E_{S1\,theory}$ = 2.16 eV) and **2PXZ-BP-F** (E_g = 2.13 eV *vs.* $E_{S1\,theory}$ = 1.89 eV) were found to be larger than those calculated. The photoluminescence quantum yields, Φ_{PL}, in degassed toluene solution of **2DTCz-BP-F**, **2DMAC-BP-F**, and **2PXZ-BP-F** are 51%, 30%, and 8%, respectively. These dropped to 49%, 21%, and 6% upon exposure to oxygen (Table 2). The prompt fluorescence and phosphorescence spectra of all compounds in 2-MeTHF at 77 K were measured to determine the S$_1$ and T$_1$ energies from their respective onsets (Fig. 5b and Fig. S18b, ESI,† Table 2). The S$_1$ energies of **2DTCz-BP-F**, **2DMAC-BP-F**, and **2PXZ-BP-F** are 2.64 eV, 2.47 eV, and 2.23 eV, and the T$_1$ energies are 2.21 eV, 2.27 eV, and 2.28 eV, respectively. The phosphorescence spectra of **2DTCz-BP-F** and **2DMAC-BP-F** are structured, and each is assigned from TDDFT calculations as a mixed locally excited triplet (^{3}LE) state of the acceptor (**BP-F**) and charge-transfer (^{3}CT) state (see Fig. S18a and Table S4, ESI†). The phosphorescence spectrum of **2PXZ-BP-F** is structureless to a mainly charge-transfer (^{3}CT) state. The ΔE_{ST} of **2DTCz-BP-F**, **2DMAC-BP-F** is 0.43 eV and 0.20 eV, respectively. The phosphorescence spectrum of **2PXZ-BP-F** in 2-MeTHF (Fig. 5 and Fig. S18b, ESI†) is slightly blue-shifted compared to the prompt fluorescence, leading to an apparent ΔE_{ST} of −0.05 eV, indicating that the emission from these two states results from different conformers. To understand how the solvent polarity affects the energies of S$_1$ and T$_1$ for **2PXZ-BP-F**, we measured the prompt fluorescence and phosphorescence spectra in hexane at 77 K, and the ΔE_{ST} is 0.05 eV for **2PXZ-BP-F** (Fig. 5b bottom). We measured the PL decays of all molecules in toluene under degassed conditions using time-correlated single-photon counting (TCSPC, Fig. S19, ESI†). The ICT band of **2DMAC-BP-F** and **2PXZ-BP-F** decays with biexponential kinetics with prompt fluorescence lifetimes, τ_p, of 27.7 ns and 16.9 ns, and delayed fluorescence lifetimes, τ_d, of 19.0 μs and 0.2 μs, respectively (Fig. S19, ESI† and Table 2). The delayed emission is strongly quenched upon the exposure of oxygen, indicating accessible triplet states. The ICT band of **2DTCz-BP-F** decays monoexponentially with τ_p of 6.6 ns, no delayed emission is observed for this compound.

To assess the emission properties of these emitters in the solid-state, their photophysical properties were first investigated in PMMA. The PL spectra are unstructured with λ_{PL} at 524, 588, and 615 nm for **2DTCz-BP-F**, **2DMAC-BP-F**, and **2PXZ-BP-F**, respectively (Fig. S20, ESI† and Table 2). The optimized Φ_{PL} in doped PMMA films under an N$_2$ atmosphere are 29%, 48%, and 28%, respectively, for **2DTCz-BP-F** (5% in PMMA), **2DMAC-BP-F** (10% in PMMA), and **2PXZ-BP-F** (1.5% in PMMA). The Φ_{PL} values were reduced to 27%, 34%, and 17%, respectively, under air. Multiexponential decay kinetics were observed in the time-resolved decays with average τ_d values of 10.1 ms, 5.0 ms, and 2.99 μs for **2DTCz-BP-F**, **2DMAC-BP-F**, and
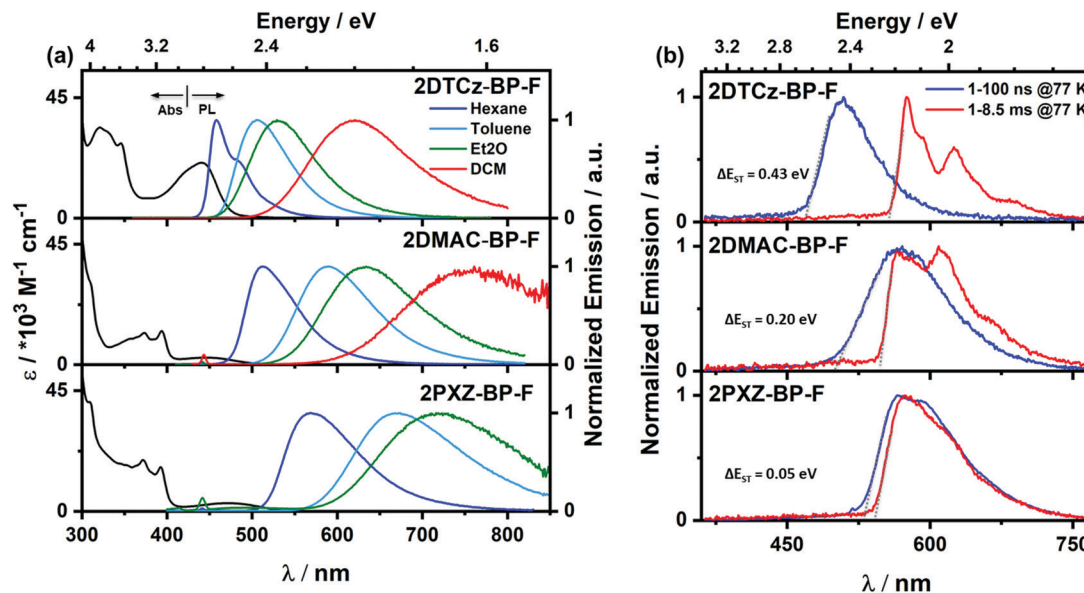
Fig. 5 (a) UV-vis absorption and PL solvatochromism study (λ_{exc} = 343 nm); (b) prompt fluorescence (blue line) and phosphorescence (red line) spectra of **2DTCz-BP-F** and **2DMAC-BP-F** in 2-MeTHF, **2PXZ-BP-F** in hexane at 77 K (λ_{exc} = 343 nm, prompt and delayed fluorescence spectra were obtained in the 1–100 ns and 1–8.5 ms time range, respectively). Et$_2$O = diethyl ether; DCM = dichloromethane.

2PXZ-BP-F, respectively (Fig. S21, ESI† and Table 2). These data are consistent with TADF being operative for the emitters in PMMA films. The S_1/T_1 energy levels of **2DTCz-BP-F** (2.56/2.22 eV), **2DMAC-BP-F** (2.56/2.28 eV), and **2PXZ-BP-F** (2.34/2.28 eV) in PMMA films are estimated from the onsets of the fluorescence and phosphorescence spectra at 77 K (Fig. S22d–f, ESI†). As a result, **2PXZ-BP-F** (0.06 eV) has the smallest ΔE_{ST} while **2DMAC-BP-F** (0.28 eV) and **2DTCz-BP-F** (0.34 eV) show significantly larger singlet–triplet gaps.

We next measured the photophysical properties of all three compounds in an OLED-relevant host 3,3′-di(9H-carbazol-9-yl)-1,1′-biphenyl (mCBP) as this host matrix has sufficiently high triplet energy (T_1 = 2.84 eV) to confine the excitons onto the emitter.[28] The dopant concentration was varied from 1–10 wt% in doped film to optimize the Φ_{PL} (Table S5, ESI†). The Φ_{PL} of the 5 wt% **2DTCz-BP-F** in mCBP doped film is 59.7% at λ_{PL} of 522 nm; 10 wt% **2DMAC-BP-F** in mCBP doped film is 78.0% at λ_{PL} of 584 nm, and 1.5 wt% **2PXZ-BP-F** in mCBP doped film is 58.0% at λ_{PL} of 611 nm under an N_2 atmosphere (Table 2). These Φ_{PL} values decreased in air to 46.8% for **2DTCz-BP-F**, 48.3% for **2DMAC-BP-F**, and 47.3% for **2PXZ-BP-F**. All three compounds show unstructured CT-based emission in mCBP doped film at room temperature, shown in Fig. S22a–c (ESI†). As shown in Fig. 6, all three compounds showed multiexponential decay kinetics with average prompt fluorescence lifetimes, average τ_p, of 4.3 ns, 19.6 ns, and 31.0 ns and average delayed emission lifetimes, average τ_d, of 10.15 ms, 90.6 μs and 1.83 μs at room temperature for **2DTCz-BP-F**, **2DMAC-BP-F**, and **2PXZ-BP-F**, respectively. The corresponding rate constants of intersystem crossing (k_{ISC}) for the three compounds in mCBP films are 1.09×10^8 s^{-1}, 2.45×10^7 s^{-1}, 1.52×10^7 s^{-1} for **2DTCz-BP-F**, **2DMAC-BP-F**, and **2PXZ-BP-F**, respectively. The rate constants of reverse intersystem crossing (k_{RISC}) in mCBP

films for **2PXZ-BP-F** reached 2.41×10^5 s^{-1}, a value much faster than **2DTCz-BP-F** of 5.14×10^1 s^{-1}, and **2DMAC-BP-F** of 1.33×10^4 s^{-1}, respectively. The relative intensities of the delayed PL increased with increasing temperature from 100 K to 300 K, thereby corroborating the TADF nature of the emission of these three compounds in the mCBP films. The extremely long lifetime and sharp decrease of the emission intensity at low temperature for the **2DTCz-BP-F** doped mCBP film can be explained by the large ΔE_{ST} (vide infra) and inefficient TADF.

There is an expectedly large ΔE_{ST} of 0.30 eV for **2DTCz-BP-F**, while the ΔE_{ST} for **2DMAC-BP-F** and **2PXZ-BP-F** is much smaller at 0.11 eV, and 0.02 eV, respectively. The S_1 level of **2DTCz-BP-F** in mCBP doped film (S_1 = 2.54 eV) is similar to the S_1 level of **2DTCz-BP-F** in PMMA doped film (S_1 = 2.56 eV) and very close to the energy level of **2DTCz-BP-F** in 2-MeTHF glass (S_1 = 2.64 eV), all of which indicates that the S_1 state in **2DTCz-BP-F** is of mixed ^{1}LE and ^{1}CT character. The structured phosphorescence and triplet energy level of **2DTCz-BP-F** does not change in different media such as PMMA (T_1 = 2.22 eV, Fig. S22d, ESI†), mCBP (T_1 = 2.24 eV, Fig. S22a, ESI†), and in 2-MeTHF glass (T_1 = 2.21 eV, Fig. 5b). Furthermore, these values match with the phosphorescence of the F-BP acceptor (2.26 eV) in 2-MeTHF glass (Fig. S18a, ESI†) and imply that the T_1 level of **2DTCz-BP-F** has ^{3}LE character. The calculated ΔE_{ST} value of **2DTCz-BP-F** in PMMA is 0.34 eV and 0.30 eV in mCBP, values that render TADF inefficient. The weak emission band at 522 nm in the millisecond timescale spectra of **2DTCz-BP-F** in mCBP and PMMA may be due to residual delayed fluorescence.

The S_1 levels of the other two emitters **2DMAC-BP-F** and **2PXZ-BP-F** in PMMA are 2.56 eV and 2.34 eV, which are significantly blue-shifted in comparison to those in mCBP doped films, for which the S_1 level for **2DMAC-BP-F** is 2.40 eV, and for **2PXZ-BP-F** is 2.22 eV. The T_1 level of **2DMAC-BP-F** is

Table 2 Photophysical properties of **2DTCz-BP-F**, **2DMAC-BP-F**, and **2PXZ-BP-F**

Emitter	λ_{PL} [nm]	τ_p [ns]	τ_d [µs]	S_1/T_1 [eV]	ΔE_{ST} [eV]	Φ_{PL} [%]
In solution						
2DTCz-BP-F	505[a]	6.6[a]	—	2.64/2.21[b]	0.43[b]	51 (49)[a]
2DMAC-BP-F	589[a]	27.7[a]	19.0[a]	2.47/2.27[b]	0.20[b]	30 (21)[a]
2PXZ-BP-F	674[a]	16.9[a]	0.2[a]	2.23/2.28[b]	−0.05[b]	8 (6)[a]
In PMMA[c]						
2DTCz-BP-F (5 wt%)	524	—	10105[d]	2.56/2.22	0.34	29 (27)[e]
2DMAC-BP-F (10 wt%)	588	—	5033[d]	2.56/2.28	0.28	48 (34)[e]
2PXZ-BP-F (1.5 wt%)	615	—	2.99[d]	2.34/2.28	0.06	28 (17)[e]
In mCBP[c]						
2DTCz-BP-F (5 wt%)	522	4.3[d]	10152[d]	2.54/2.24	0.30	60 (47)[e]
2DMAC-BP-F (10 wt%)	584	19.6[d]	90.6[d]	2.40/2.29	0.11	78 (48)[e]
2PXZ-BP-F (1.5 wt%)	611	31.0[d]	1.83[d]	2.22/2.20	0.02	58 (47)[e]

[a] At 298 K, values quoted are in degassed toluene solutions prepared by three freeze–pump–thaw cycles: for λ_{PL} the λ_{exc} = 343 nm for **2DTCz-BP-F**, λ_{exc} = 391 nm for **2DMAC-BP-F** and **2PXZ-BP-F**. For lifetime λ_{exc} = 379 nm. Φ_{PL} values inside parenthesis quoted after aeration of a toluene solution. [b] Obtained from the onset of the prompt fluorescence (time window: 1–100 ns) and phosphorescence spectra (time window: 1–8.5 ms) measured in 2-MeTHF glass at 77 K, λ_{exc} = 343 nm. [c] Thin films of PMMA and mCBP were prepared by spin-coating. Steady-state and time-resolved emission spectra were recorded at 298 K under an O$_2$-free atmosphere (λ_{exc} = 343 nm for steady-state and λ_{exc} = 379 nm for time-resolved emission). [d] Average lifetime ($\tau_{avg} = \sum A_i\tau_i^2/\sum A_i\tau_i$, where A_i is the pre-exponential for lifetime τ_i). Prompt and delayed emissions were measured by TCSPC and MCS, respectively (λ_{exc} = 343 nm). [e] Photoluminescence quantum yields of thin films were determined using an integrating sphere (λ_{exc} = 305 nm or 340 nm) under N$_2$ atmosphere at 298 K. Values quoted inside the parentheses are in the presence of O$_2$.

2.29 eV, very similar to that in PMMA (2.28 eV for **2DMAC-BP-F**) and a value that aligns with the T$_1$ level of the BP-F acceptor in 2-MeTHF (2.26 eV, Fig. S18a, ESI†). However, the T$_1$ level of **2PXZ-BP-F** in mCBP is 2.20 eV, which is stabilized from the value measured in PMMA at 2.28 eV (Fig. S22f, ESI† and Table 2). These results reveal that the T$_1$ state in **2DMAC-BP-F** possesses dominant ^{3}LE character, while **2PXZ-BP-F** shows mainly ^{3}CT character. The estimated ΔE_{ST} of **2DMAC-BP-F** is 0.11 eV, and of **2PXZ-BP-F** is 0.02 eV in mCBP, while the ΔE_{ST} in PMMA of **2DMAC-BP-F** is 0.28 eV, and of **2PXZ-BP-F** is 0.06 eV, which is suitably small for harvesting triplet excitons. Indeed, the small ΔE_{ST} of **2DMAC-BP-F** and **2PXZ-BP-F** is a sign of an efficient TADF emitter for OLEDs.

Device characterization

OLED devices based on **2PXZ-BP-F**, **2DMAC-BP-F** and **2DTCz-BP-F** were fabricated by vacuum deposition following a typical bottom-emitting OLED device architecture (Fig. 7a) that consists of indium tin oxide (ITO)/1,4,5,8,9,11-hexaazatriphenylene-hexacarbonitrile (HATCN) (5 nm)/N,N′-di(1-naphthyl)-N,N′-diphenyl-(1,1′-biphenyl)-4,4′-diamine (NPB) (40 nm)/tris(4-carbazoyl-9-ylphenyl)amine (TCTA) (10 nm)/emissive layer (20 nm)/1,3,5-tri[(3-pyridyl)-phen-3-yl]benzene (TmPyPB) (40 nm)/LiF (0.6 nm)/Al (100 nm), where HATCN, NPB and TCTA play the role of hole injection layer (HIL), hole transportation layer (HTL) and electron blocker layer (EBL), respectively. TmPyPB acts both as electron transport layer (ETL) and hole blocking layer due to its deep HOMO (−6.7 eV),[29] and LiF acts as an electron injection layer (EIL). The molecular structures of the materials used in these OLEDs are shown in Fig. 7b. The emission layer (EML) comprises 1.5 wt% of **2PXZ-BP-F**, 10 wt% **2DMAC-BP-F**, or 5 wt% of **2DTCz-BP-F** doped into mCBP, based on the doping study discussed above (Table S5, ESI†). The performance of the OLEDs is summarized in Table 3. Current density–voltage–brightness (J–V–L) curves, EQE–luminance curves, and electroluminescence spectra (EL) are given in Fig. 7c. As shown in Fig. 7e, each EL spectrum is similar to that of the corresponding PL spectrum in the thin film with EL maxima, λ_{EL}, at 605 nm for **2PXZ-BP-F**, 585 nm for **2DMAC-BP-F**, and 518 nm for **2DTCz-BP-F**. Similar to that observed by PL, the trend in emission energy follows that of increasing donor strength. The corresponding CIE coordinates are (0.55, 0.44), (0.51, 0.48) and (0.29, 0.58) for the devices with **2PXZ-BP-F**, **2DMAC-BP-F** and **2DTCz-BP-F**, respectively. The turn-on voltage of the devices lies between 3.3 V to 3.7 V and is dependent on the energy gap between the HOMO of materials used in HTL and EML layers. The **2DMAC-BP-F** based device showed the best overall performance with the highest maximum external quantum efficiency (EQE$_{max}$) of 21.8%, a maximum current efficiency (CE$_{max}$) of 59.7 cd A^{-1}, and maximum power efficiency (PE$_{max}$) of 55.4 lm W^{-1} (Table 3, Fig. 7d and Fig. S23 and S24, ESI†). The EQE$_{max}$ of the **2PXZ-BP-F**-based device is 12.4% with CE$_{max}$ = 26.3 cd A^{-1} and PE$_{max}$ = 23.0 lm W^{-1}. The **2PXZ-BP-F**-based device showed moderate roll-off efficiency, with the EQE at 100 cd m^{-2} at 9.3% and the EQE at 1000 cd m^{-2} at 6.3%. The **2DMAC-BP-F**-based device, however, showed higher efficiency roll-off, with an EQE at 100 cd m^{-2} of 8.7% and an

Fig. 6 Temperature-dependent time-resolved PL decay of (a) 5 wt% **2DTCz-BP-F** doped mCBP film; (b) 10 wt% **2DMAC-BP-F** doped mCBP film; (c) 1.5 wt% **2PXZ-BP-F** doped mCBP film (λ_{exc} = 379 nm).

4764 | *J. Mater. Chem. C*, 2022, **10**, 4757–4766

This journal is © The Royal Society of Chemistry 2022

Fig. 7 (a) Energy level diagram of materials employed in the devices; (b) molecular structure of materials used in the devices; (c) current density and luminance *versus* voltage characteristics for the devices; (d) external quantum efficiency *versus* luminance curves for the devices, the inset is the electroluminescence of **2PXZ-BP-F**, **2DMAC-BP-F**, and **2DTCz-BP-F**; (e) electroluminescence spectra of the device.

Table 3 Electroluminescence data for the devices[a]

Emitter	Host	V_{on}[b] [V]	λ_{EL}[c] [nm]	CE[d] [cd A^{-1}]	PE$_{max}$ [lm W^{-1}]	EQE[d] [%]	CIE[c] [x,y]
2PXZ-BP-F	mCBP (1.5%)	3.3	605	26.3/19.1/12.7	23.0	12.4/9.3/6.3	0.549, 0.444
2DMAC-BP-F	mCBP (10%)	3.6	585	59.7/23.5/8.1	55.4	21.8/8.7/3.3	0.513, 0.479
2DTCz-BP-F	mCBP (5%)	3.7	518	6.7/3.7/3.0	5.6	2.1/1.2/1.0	0.290, 0.580

[a] Device stacks; ITO/HATCN (5 nm)/NPB (40 nm)/TCTA (10 nm)/emissive layer (20 nm)/TmPyPB (40 nm)/LiF (0.6 nm)/Al (100 nm). [b] The turn-on voltage at a brightness 1 cd m^{-2}. [c] The electroluminescence maximum and CIE coordinates recorded at 5 V. [d] The order of measured values: the maximum EQE/EQE at 100 cd m^{-2}/EQE at 1000 cd m^{-2}.

EQE of 1000 cd m^{-2} at 3.3%. The maximum brightness of the **2PXZ-BP-F**-based device reached 12 350 cd m^{-2} at an EQE of 2.3%. The relatively low efficiency roll-off in **2PXZ-BP-F** originates in part from the low triplet exciton concentration due to the relatively short delayed lifetime (τ_d = 1.83 μs).[30,31] Notably, the **2PXZ-BP-F**-based device reached an EQE of 2.5% at 10 000 cd m^{-2} with an emission wavelength beyond 600 nm. Although **2DTCz-BP-F** shows a high Φ_{PL} of *ca.* 60% in the 5 wt% doped in mCBP, the device exhibits a low EQE$_{max}$ of 2.1%. As a result of the too high ΔE_{ST}, the harvesting of triplet excitons in the **2DTCz-BP-F**-based device is very inefficient as reflected in the very long delayed lifetime, which causes more triplet–triplet annihilation and triplet–polaron annihilation. Devices fabricated using MoO$_3$ as the HIL showed similar performance but reached lower luminance and low current density than the devices using HATCN (Table S6 and Fig. S25, ESI†).

Conclusions

This study reported a series of green-to-red-emitting fluorine-substituted dibenzo[*a,c*]phenazine-based (**BP-F**) TADF emitters. **2DTCz-BP-F**, **2DMAC-BP-F**, and **2PXZ-BP-F**, which showed color tuning based on the choice of donor, emitting from green to deep-red.

The rigid and planar constituent groups with large steric hindrance between donor and acceptor units endow these emitters with high Φ_{PL} vlues and suitably small ΔE_{ST}. Among them, **2DMAC-BP-F** exhibits the highest Φ_{PL}, at 78%, a relatively small ΔE_{ST} of 0.11 eV at 584 nm in 10 wt% doped mCBP, whereas **2PXZ-BP-F** shows the smallest ΔE_{ST} of 0.02 eV with shortest delay lifetime of 1.83 μs at 611 nm in 1.5 wt% doped mCBP. OLED devices using these TADF materials showed excellent performance with an EQE$_{max}$ of 21.8% in the case of **2DMAC-BP-F** with λ_{EL} of 585 nm and 12.4% for **2PXZ-BP-F** with λ_{EL} of 605 nm. The relatively low efficiency roll-off in **2PXZ-BP-F** is due to the short delayed lifetime, making this material a very good TADF emitter for OLEDs in the family of devices that can reach brightness above 10 000 cd m^{-2} with an emission wavelength beyond 600 nm. These results demonstrate that simple modification of the BP acceptor with a fluorine substituent is an effective approach to design orange-red/red TADF emitters with devices that show high EQE and low-efficiency roll-off.

Data availability

The research data supporting this publication can be accessed at https://doi.org/10.17630/2553f890-29d1-4fb8-a49c-0cf06404d856.

Conflicts of interest

The authors declare no conflict of interest.

Acknowledgements

References

1 M. Y. Wong and E. Zysman-Colman, *Adv. Mater.*, 2017, **29**, 1605444.

2 G. Hong, X. Gan, C. Leonhardt, Z. Zhang, J. Seibert, J. M. Busch and S. Brase, *Adv. Mater.*, 2021, **33**, e2005630.

3 P. de Silva, C. A. Kim, T. Zhu and T. Van Voorhis, *Chem. Mater.*, 2019, **31**, 6995–7006.

4 J. X. Chen, W. W. Tao, W. C. Chen, Y. F. Xiao, K. Wang, C. Cao, J. Yu, S. Li, F. X. Geng, C. Adachi, C. S. Lee and X. H. Zhang, *Angew. Chem., Int. Ed.*, 2019, **58**, 14660–14665.

5 J. Xue, Q. Liang, R. Wang, J. Hou, W. Li, Q. Peng, Z. Shuai and J. Qiao, *Adv. Mater.*, 2019, **31**, e1808242.

6 R. Englman and J. Jortner, *Mol. Phys.*, 1970, **18**, 145–164.

7 J. V. Caspar, E. M. Kober, B. P. Sullivan and T. J. Meyer, *J. Am. Chem. Soc.*, 2002, **104**, 630–632.

8 J. Eng and T. J. Penfold, *Chem. Rec.*, 2020, **20**, 831–856.

9 J. H. Kim, J. H. Yun and J. Y. Lee, *Adv. Opt. Mater.*, 2018, **6**, 1800255.

10 Q. Zhang, H. Kuwabara, W. J. Potscavage, Jr., S. Huang, Y. Hatae, T. Shibata and C. Adachi, *J. Am. Chem. Soc.*, 2014, **136**, 18070–18081.

11 W. Zeng, H. Y. Lai, W. K. Lee, M. Jiao, Y. J. Shiu, C. Zhong, S. Gong, T. Zhou, G. Xie, M. Sarma, K. T. Wong, C. C. Wu and C. Yang, *Adv. Mater.*, 2018, **30**, 1704961.

12 L. Yu, Z. Wu, G. Xie, W. Zeng, D. Ma and C. Yang, *Chem. Sci.*, 2018, **9**, 1385–1391.

13 F. M. Xie, P. Wu, S. J. Zou, Y. Q. Li, T. Cheng, M. Xie, J. X. Tang and X. Zhao, *Adv. Electron. Mater.*, 2020, **6**, 1900843.

14 F. M. Xie, H. Z. Li, G. L. Dai, Y. Q. Li, T. Cheng, M. Xie, J. X. Tang and X. Zhao, *ACS Appl. Mater. Interfaces*, 2019, **11**, 26144–26151.

15 S. Kothavale, W. J. Chung and J. Y. Lee, *ACS Appl. Mater. Interfaces*, 2020, **12**, 18730–18738.

16 Y. Liu, Y. Chen, H. Li, S. Wang, X. Wu, H. Tong and L. Wang, *ACS Appl. Mater. Interfaces*, 2020, **12**, 30652–30658.

17 C. Adamo and V. Barone, *J. Chem. Phys.*, 1999, **110**, 6158–6170.

18 S. Grimme, *Chem. Phys. Lett.*, 1996, **259**, 128–137.

19 S. Hirata and M. Head-Gordon, *Chem. Phys. Lett.*, 1999, **314**, 291–299.

20 N. G. Connelly and W. E. Geiger, *Chem. Rev.*, 1996, **96**, 877–910.

21 A. J. Bard and L. R. Faulkner, *Electrochemical Methods: Fundamentals and Applications*, John Wiley & Sons, 1980.

22 M. Thelakkat and H.-W. Schmidt, *Adv. Mater.*, 1998, **10**, 219–223.

23 J. L. Brédas, R. Silbey, D. S. Boudreaux and R. R. Chance, *J. Am. Chem. Soc.*, 2002, **105**, 6555–6559.

24 S. Kothavale, W. J. Chung and J. Y. Lee, *J. Mater. Chem. C*, 2020, **8**, 7059–7066.

25 J. X. Chen, K. Wang, C. J. Zheng, M. Zhang, Y. Z. Shi, S. L. Tao, H. Lin, W. Liu, W. W. Tao, X. M. Ou and X. H. Zhang, *Adv. Sci.*, 2018, **5**, 1800436.

26 Y.-Y. Wang, Y.-L. Zhang, K. Tong, L. Ding, J. Fan and L.-S. Liao, *J. Mater. Chem. C*, 2019, **7**, 15301–15307.

27 J. X. Chen, W. W. Tao, Y. F. Xiao, K. Wang, M. Zhang, X. C. Fan, W. C. Chen, J. Yu, S. Li, F. X. Geng, X. H. Zhang and C. S. Lee, *ACS Appl. Mater. Interfaces*, 2019, **11**, 29086–29093.

28 S. Gong, X. He, Y. Chen, Z. Jiang, C. Zhong, D. Ma, J. Qin and C. Yang, *J. Mater. Chem.*, 2012, **22**, 2894–2899.

29 S. J. Su, T. Chiba, T. Takeda and J. Kido, *Adv. Mater.*, 2008, **20**, 2125.

30 A. K. Gupta, W. Li, A. Ruseckas, C. Lian, C. L. Carpenter-Warren, D. B. Cordes, A. M. Z. Slawin, D. Jacquemin, I. D. W. Samuel and E. Zysman-Colman, *ACS Appl. Mater. Interfaces*, 2021, **13**, 15459–15474.

31 N. C. Giebink and S. R. Forrest, *Phys. Rev. B: Condens. Matter Mater. Phys.*, 2008, **77**, 235215.

4766 | *J. Mater. Chem. C*, 2022, **10**, 4757–4766

This journal is © The Royal Society of Chemistry 2022